ADVANCING EARTH AND SPACE SCIENCES

JGR Atmospheres

RESEARCH ARTICLE
10.1029/2024JD042787

Special Collection:
Southern Ocean clouds, aerosols, precipitation and radiation

Key Points:

- Measurements on King George Island from 2017 to 2023 are used to characterize Southern Ocean clouds and radiation over the annual cycle
- The cloud fraction over King George Island in the Southern Ocean is found to be 96% with 86% of the lowest cloud bases within the first 1 km
- Monthly average downward cloud forcing over King George Island varies from −116 to 63 W m^{-2} and is negative from October to March and positive from April to September

Supporting Information:

Supporting Information may be found in the online version of this article.

Correspondence to:

P. M. Rowe,
penny@nwra.com

Citation:

Rowe, P. M., Zou, X., Gorodetskaya, I., Stillwell, R. A., Cordero, R. R., Sepulveda, E., et al. (2025). Observations of clouds and radiation over King George Island and implications for the Southern Ocean and Antarctica. *Journal of Geophysical Research: Atmospheres*, *130*, e2024JD042787. https://doi.org/10.1029/2024JD042787

Received 23 OCT 2024
Accepted 17 JUL 2025

Author Contributions:

Conceptualization: Penny M. Rowe
Data curation: Penny M. Rowe
Formal analysis: Penny M. Rowe, Robert A. Stillwell
Funding acquisition: Penny M. Rowe, Xun Zou, Irina Gorodetskaya, Robert

Observations of Clouds and Radiation Over King George Island and Implications for the Southern Ocean and Antarctica

Penny M. Rowe[1], Xun Zou[2], Irina Gorodetskaya[3], Robert A. Stillwell[4], Raul R. Cordero[5], Edgardo Sepulveda[5,6], David H. Bromwich[7], Zhenhai Zhang[2], F. Martin Ralph[2], and Steven Neshyba[8]

[1]NorthWest Research Associates, Seattle, WA, USA, [2]CW3E, Scripps Institution of Oceanography, University of California San Diego, La Jolla, CA, USA, [3]CIIMAR | Interdisciplinary Centre of Marine and Environmental Research, University of Porto, Porto, Portugal, [4]NSF National Center for Atmospheric Research, Earth Observing Lab, Boulder, CO, USA, [5]University of Santiago of Chile, Santiago, Chile, [6]Chemical and Environmental Engineering Department, University of Arizona, Tucson, AZ, USA, [7]Polar Meteorology Group, Byrd Polar and Climate Research Center, The Ohio State University, Columbus, OH, USA, [8]University of Puget Sound, Tacoma, WA, USA

Abstract Clouds play an important role in the Southern Ocean and Antarctic surface energy balance via their radiative effects and in surface mass balance via precipitation formation. Here, we use measurements at Escudero Station (62.2°S, 58.97°W) on King George Island, north of the Antarctic Peninsula, to characterize clouds and their effects on the surface incoming radiation between 2017 and 2023. These measurements are unique providing 7 years of simultaneous cloud and radiation measurements, including year-round observations. Cloud measurements using a mini micropulse lidar showed that clouds are present 96% of the time with persistent low-level supercooled liquid-containing clouds: 86% of the lowest cloud bases are within the first 1 km. Liquid was present about 80% of the time, and most liquid was supercooled: cloud-base temperatures were below 0°C for 82% of atmospheric columns classified as liquid-containing. Combining pyranometer and pyrgeometer measurements with clear-sky radiative transfer modeling, we find that the downward cloud radiative forcing is negative during October–March and positive during April–September. For clouds with base temperatures below 260 K, downward longwave cloud forcing is found to be lower for ice-only clouds than for liquid-containing clouds; however, at warmer temperatures, both ice-only and liquid-containing clouds exhibited similar radiative forcing. During strong atmospheric river (AR) events, when long corridors of moisture bring heat and precipitation, surface temperatures are found to be positively correlated with downward shortwave (DSW) cloud forcing in summer, indicating that weaker DSW cloud forcing is linked to higher summertime surface temperatures.

Plain Language Summary The Southern Ocean is one of the cloudiest places on Earth. The clouds there play an important but complex role in the Antarctic climate, causing cooling by reflecting sunlight back to space but also warming by trapping infrared radiation emitted by the surface. The overall effect depends on time of year, time of day, and the characteristics of the cloud—how high they are and whether they are made of liquid, ice or a mix of both. Using measurements made at the research station Escudero, located on an island in the Southern Ocean, just north of the Antarctic Peninsula, we characterize clouds from 2017 to 2023. Our measurements showed mostly cloudy conditions with clouds present 96% of the time. A large fraction of the clouds, we observed were very low. Temperatures at the cloud bases tend to be just below freezing. Because the air is so clean at this remote Antarctic location, most of the clouds contain liquid despite temperatures at the cloud base being below 0°C (32 Fahrenheit). Overall, at this location, clouds cause a cooling effect on the surface in summer and a warming effect during other seasons.

1. Introduction

Clouds have a major impact on the climate of the Southern Ocean (SO) and Antarctic Peninsula (AP). Through their interactions with radiation, clouds modulate the surface energy budget. Sato and Simmonds (2021) found that increases in downward longwave radiation linked to increases in cloud amount and air temperature were key to surface warming in autumn and winter over the AP during 1950–2020. Complicating the picture, the longwave warming effect of clouds is opposed by a shortwave cooling effect. For example, in February 2022, during a

A. Stillwell, F. Martin Ralph, Steven Neshyba
Investigation: Penny M. Rowe, Xun Zou, Irina Gorodetskaya, Raul R. Cordero, Edgardo Sepulveda, Zhenhai Zhang
Methodology: Penny M. Rowe, Xun Zou, Irina Gorodetskaya
Writing – original draft: Penny M. Rowe
Writing – review & editing: Xun Zou, Robert A. Stillwell, Raul R. Cordero, Edgardo Sepulveda, David H. Bromwich, Zhenhai Zhang, Steven Neshyba

combined Atmospheric River (AR) and Foehn event, clouds enhanced the downwelling infrared radiation over the SO and western AP, whereas cloud-clearing through the Foehn effect allowed significant shortwave radiation to reach the surface on the lee side of the AP leading to warming and melting (Gorodetskaya et al., 2023; Zou et al., 2023).

Improved knowledge of Antarctic clouds is needed to address major biases in climate, reanalysis, and numerical weather prediction models (Bodas-Salcedo et al., 2012, 2014; Fiddes et al., 2022; Haynes et al., 2011; Hyder et al., 2018; Trenberth et al., 2010). Errors include underestimating SO and coastal Antarctic cloud fractions (Bodas-Salcedo et al., 2012; Trenberth et al., 2010), incorrectly representing secondary ice production (Grosvenor et al., 2012; O'Shea et al., 2017), and incorrectly simulating the radiative fluxes at the surface of the Southern Ocean (McFarquhar et al., 2021) primarily due to the challenges in predicting the ubiquitous mixed phase clouds. Taken together, these point to a continued need for surface-based measurements to characterize clouds over Antarctica and the SO and evaluate satellite-based retrievals and model results.

Cloud properties that are particularly important to measure include cloud amount, thermodynamic phase, and height, which significantly affect Antarctic net radiation (e.g., Gilbert et al., 2020; Lubin et al., 2020). Low-level supercooled liquid clouds are ubiquitous over the AP and SO (Hu et al., 2010; Huang et al., 2012), where they have been implicated in warming events (Bromwich et al., 2020; Gorodetskaya et al., 2023). Compared to ice clouds, liquid clouds in Antarctica tend to be optically thicker (Lubin et al., 2015), which enhances both shortwave reflectivity (Haynes et al., 2011) and longwave emissivity with opposite effects on the downward radiative flux. The higher temperatures typical of low clouds increase their downwelling longwave radiation, mitigating radiative energy loss at the surface. Indeed, within the near-surface temperature inversions common in polar regions, cloud temperatures higher than the surface temperature can result in positive net surface longwave radiation (Wille et al., 2024).

ARs and Foehn events impact cloud formation and therefore affect downwelling radiative fluxes. ARs are long corridors of moisture that bring heat and precipitation to the Antarctic region and can lead to additional cloud formation (Gorodetskaya et al., 2023). In summer, when there is a lot of solar radiation, clouds primarily cause a cooling effect by blocking solar radiation (Trenberth et al., 2010; Zou et al., 2023). In winter, by contrast, when levels of solar radiation are low, the warming effect due to longwave radiation from clouds has a much greater relative effect. Further complicating matters, Foehn events, which can be triggered by ARs, often lead to additional cloud formation on the upwind side of the Antarctic Peninsula with cloud clearance on the lee side (Bozkurt et al., 2018; Gorodetskaya et al., 2023; Wille et al., 2019; Zou et al., 2023). Surface-based measurements during AR and Foehn events are needed to improve our understanding of the radiative effect of clouds on the surface particularly on the SO near the Antarctic Peninsula where surface-based measurements are infrequent.

Most observations of SO clouds and surface radiation fluxes are based upon ship cruises or campaigns of limited duration. The exception is the Macquarie Island Cloud and Radiation Experiment (MICRE) that ran for 2 years at 54.5°S (Tansey et al., 2023). Situated on an island in the Southern Ocean north of the AP at 62.2°S, Escudero Station on King George Island (KGI; see Figure 1) is expected to have significantly more low cloud cover than Macquarie Island (Listowski et al., 2019; Tansey et al., 2023). KGI is exposed to the circumpolar westerly winds from the South Pacific Ocean so its point observations of clouds and radiation for the full annual cycle implicitly are representative of these phenomena across extensive high-latitude areas. Further, it is located in the vicinity of the northern edge of the Antarctic sea ice zone where it is imperative to know the downward longwave radiative flux from the atmosphere to the surface that plays a central role in determining the expansion of the sea ice cover (Cerovecki et al., 2022). For exploring the role of ARs and Foehn, KGI is situated on the upwind side where both are expected to lead to additional cloud formation.

Here, we characterize the annual cycle of clouds and downwelling radiation over the SO using measurements made at Escudero Station on KGI over 7 years between 2017 and 2023. In particular, we use surface-based mini micropulse lidar (miniMPL) measurements to determine cloud height and the frequency of clear skies, ice-only clouds, and clouds containing supercooled liquid. The miniMPL is sensitive to cloud phase particularly for low clouds. Surface-based broadband radiation measurements are used to explore how cloud forcing varies with cloud properties. Finally, we explore cloud forcing during strong atmospheric rivers identified at KGI between 2017 and 2023. Measurements and methods are described in Sections 2 and 3. Sections 4–6 present results and discussion with Section 4 characterizing clouds over KGI, Section 5 describing cloud forcing over the annual cycle, and Section 6 focusing on cloud forcing during ARs. Section 7 presents conclusions.

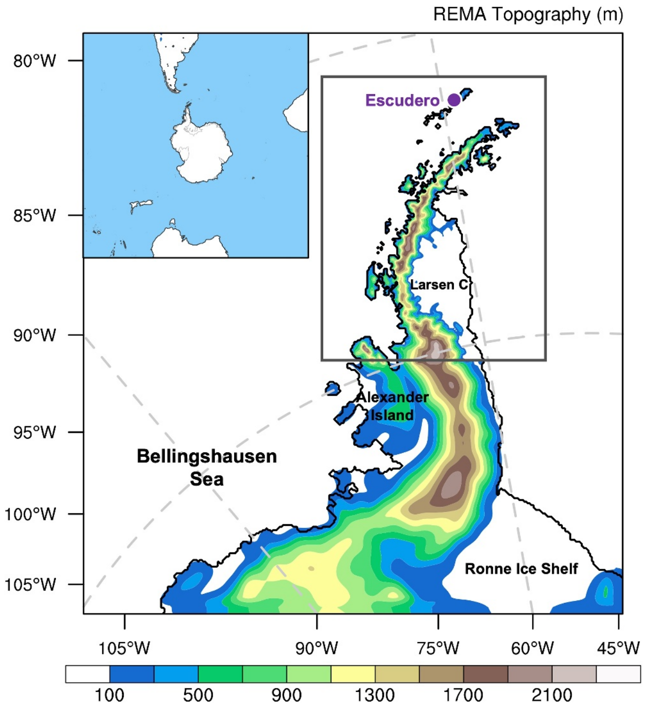

Figure 1. Map of the Antarctic Peninsula showing the location of Escudero Station. Topography map is processed based on elevation information from the Reference Elevation Model of Antarctica (REMA; Howat et al., 2019). Lines of latitude are shown at 60°S and 70°S.

2. Measurements

Downward shortwave (DSW) radiative flux was measured continuously at Escudero station from December 2016 through 2023 with a Kipp and Zonen SMP21-V global hemispherical irradiance (GHI) pyranometer sensor, which is a thermopile secondary standard sensor with a spectral range of 285–2,800 nm and less than 2 s response time. Downward longwave (DLW) radiative flux was measured continuously from Dec. 2017 through 2023 with a Kipp and Zonen SGR4-V plane surface pyrgeometer with an all-black thermoelectric detector, a spectral range of between 4,500 nm and 42,000 nm, and a response time of less than 16 s. Both sensors have a 1-min average acquisition system and are fitted with a Kipp and Zonen CVF4 ventilation unit to reduce dew, precipitation, and pollution on the domes. Domes were cleaned every two to three days and after precipitation events. Alignment checks were carried out weekly.

Lidar measurements were carried out using a SigmaSpace mini Micro Pulse Lidar (miniMPL-532-C; hereafter miniMPL), which is a polarization sensitive elastic backscatter lidar. The miniMPL has a laser emission wavelength of 532 nm, a repetition rate of 2,500 Hz, and an output energy of approximately 4 μJ per pulse. This system has been operating in Escudero Station since November 2016 and has been part of the NASA Micro-Pulse Lidar Network (MPLNET; NASA, 2023) since November 2017, with continuous operation during the Austral summer seasons as well as during the Austral winters of 2022 and 2023. The instrumentation was housed inside a heated (∼20°C) sealed enclosure, tilted slightly to avoid specular reflection from oriented ice crystals, and equipped with a fan to minimize condensation on the window. The enclosure window was cleaned periodically, particularly after precipitation events.

In addition to broadband radiation and miniMPL measurements, balloon-borne GRAW DFM-09 radiosondes equipped with temperature, relative humidity, atmospheric pressure, and GPS-based wind sensors were launched during January 2017, austral summers of 2017–2018 and 2018–2019, September 2019, and periodically during 2022 and 2023. Radiosondes typically ascended to ∼20 km before the balloon burst at an ascent speed of ∼5 m/s with ∼1 Hz data acquisition frequency, resulting in a sampling resolution of approximately 5 m. The number of radio soundings conducted each month from 2017 to 2023 used in this study, along with their observation times, is given in Table S1 in Supporting Information S1.

Surface temperature data were measured at C.M.A. Eduardo Frei Montalva (hereafter Frei) station at 62.19194°S, 58.98278°W about a mile from Escudero Station and made available by MeteoChile (https://climatologia.meteochile.gob.cl).

3. Methods

3.1. MiniMPL

MiniMPL data were processed primarily following the method of Stillwell et al. (2018). Here, we focus on the differences from this method. Measurements were acquired up to an altitude of 30 km using the SigmaSpace SigmaMPL2015 software with a resolution of 30 m and 30 s, which was then averaged to two minutes.

Afterpulse corrections and saturation corrections were made to account for nonideal detector behavior (Campbell et al., 2002). Afterpulse calibrations were performed monthly and interpolated in time for each profile. Because the saturation correction is not expected to vary in time, saturation correction curves provided by the detector manufacturer were used. Background subtraction was performed by estimating the background signal from the top 2 km of the profile where no measurable laser signal was observed. Corrected and background-subtracted photon counts were then normalized to the measured output laser power. Finally, overlap corrections were performed using manufacturer-supplied estimates of the collection efficiency of the miniMPL's telescope as a function of range.

10.1029/2024JD042787

Following the corrections for nonideal instrument behavior, observed and corrected photon counts were filtered to remove low signal-to-noise ratio observations and integrated photon count numbers less than $10^{-2.5}$ per shot were removed. Speckle filtering was then applied twice in which pixels are screened out if more than 50% of their neighbors are found to have failed quality control.

Polarization calculations followed Flynn et al. (2007) without modification. A Klett inversion (Klett, 1981) was performed on the filtered photon counts assuming a lidar ratio of 25. Fernald inversions (Fernald et al., 1972) were also performed with the same parameters to verify that results were not substantially changed by the choice of inversion. Both inversions used estimates of temperature and pressure from the European Centre for Medium-Range Weather Forecasts (ECMWF) Reanalysis version 5 (ERA5; Hersbach et al., 2020, 2023). ERA5 temperature profiles were also used to determine cloud base temperatures. The resulting polarization and backscatter ratio (defined as the ratio of observed backscattered light to the amount of light expected if backscattering occurred only from molecules) data were used for scene classification.

Scene classification was performed for all valid lidar data, assuming that the contents of any given observational region (pixel) were homogeneous. Observations (at a given range and time) were classified as clear for backscatter ratios less than 10 and otherwise cloudy. Aerosol classification was not attempted due to the limits of information content in elastic backscatter lidar. Cloudy pixels were further classified by dominant phase when possible: as ice when the depolarization was greater than 10% and errors did not exceed 5%, and as liquid for depolarizations less than 10% when the polarization error did not exceed 1%. When errors are large compared to the depolarization signal, cloud phase cannot be determined and the pixels were categorized as cloud of unknown phase. Atmospheric columns were classified as clear, obscured, or containing liquid, ice-only cloud, or unknown cloud, following Stillwell et al. (2018). The categorization of "obscured" was assigned when the lidar signal was attenuated almost immediately, indicating either instrument effects, such as the presence of condensation or precipitation on the enclosure window or geophysical effects such as fog. Note that as with all lidar systems, no information content is available beyond the range where the lidar signal is totally extinguished.

The fraction of each day when the sky was clear was calculated from the atmospheric column classifications as

$$F_{\mathrm{clr}}(\mathrm{day}) = n_{\mathrm{clr}}(\mathrm{day})/n_{\mathrm{tot}}(\mathrm{day}),$$

where $n_{\mathrm{clr}}(\mathrm{day})$ is the number of clear-sky column identifications on the given day and $\mathrm{n_{tot}}(\mathrm{day})$ is the total number of measurements in the day (typically constant). This was repeated for other column classifications: liquid-containing, ice-only, obscured, or unknown cloud. Cloud base heights were determined as the first valid altitude classified as cloudy, omitting atmospheric columns classified as obscured. For clouds classified as ice-only but with cloud base temperatures between 273 and 276 K, it was assumed that the temperature, which was taken from ERA5, was inaccurate. The assumption that ERA5 temperatures could be in error by as much as 3 K was based on comparisons of ERA5 temperature profiles to in situ temperature measurements made on radio soundings for the closest ERA5 grid location and time. The radiosonde temperatures were interpolated onto the ERA5 pressure grid. Although differences of up to 6 K were found, most differences were within ±3 K. When cloud base temperatures exceeded 276 K, it was assumed that the cloud phase classification was incorrect and such clouds were assumed to be liquid-containing; this only affected 0.4% of cloudy observations.

Monthly averages for each year were then calculated as the monthly means of daily fractions. Monthly averages for the entire period (2017/11–2023/8) were calculated as a weighted mean of monthly averages for each year, where the weights are proportional to the number of operational days (see Figure S1 in Supporting Information S1). Measurements were made during the summer in most years. For most of fall and winter (April–August), measurements were made only during 2022 and 2023. Finally, for the first months of spring (September and October), measurements were only made during 2019.

To determine the fraction of time the sky was clear, contained liquid-containing clouds, or contained ice-only clouds, the time periods when the atmospheric column was classified as obscured or containing clouds of unknown phase were ignored. Time periods for the remaining categories were normalized so that the total time was 100%. This is equivalent to making the following assumptions. First, we assume that clouds were present during time periods when the column was classified as obscured. Justification for this choice is given in Section 5.2.

Second, we calculate the ratio of liquid-containing cloud to ice-only cloud when the cloud phase is known and assume the ratio is the same for the overall time period when cloud phase is not known.

We have elected to use the phrase "liquid-containing" clouds in lieu of more common terminology such as "mixed-phase" clouds. This is because the only cloud profiling instrument operating at Escudero Station was a mini micropulse lidar; cloud radar data were not available. As lidar systems are primarily sensitive to the liquid in mixed-phase clouds, a secondary measurement is typically needed to identify ice when liquid and ice are mixed in a volume of air. When they are physically separated in space, for example, ice virga falling from a liquid cloud, we have classified that as liquid-containing, since liquid was expected to be more radiatively important.

In general, we find that for clear air, liquid-containing, ice-only, and obscured columns, most of the data is retained even for time windows of over 2 hours, providing evidence of sky homogeneity for these classifications. Thus, the small fraction of measurements in Figure 7a that have high radiative forcing for columns classified as clear air is probably attributable to inhomogeneous sky coverage. Conversely, given that more than 95% of data remains when specifying that liquid clouds must constitute the majority of observations for a 2.5 hr window, the long tail observed in Figure 7b is not likely to be attributable to the same mechanism. Finally, the "Unknown Cloud" category falls to 0% over the same 2.5 hr window. The interpretation this implies is that it is very uncommon for a cloud phase to not be classifiable for long periods of time.

It is important to note that lidar systems are fundamentally limited by the inefficient propagation of light through clouds. The lidar can only see vertically into the atmosphere until the lidar beam is extinguished. Thus, although our findings regarding the prevalence of low clouds are robust, we cannot report the frequency of high clouds over Escudero since low clouds are so ubiquitous and the lidar typically does not penetrate far enough into the atmosphere.

3.2. Clear-Sky Downwelling Longwave Radiative Fluxes

Clear-sky DLW radiation was calculated at radiosonde launch times. First, atmospheric profiles were created for 70 altitude levels from the surface to 60 km; altitudes were chosen to become progressively farther apart going up in the atmosphere. Radiosonde measurements were used for lower atmospheric temperature, pressure, and humidity profiles. Above 11.5 km, the water vapor was set to 4 ppm (Rowe et al., 2008). ERA5 pressure level data were used for temperature above the maximum radiosonde altitude as well as for the ozone profile. Carbon dioxide profiles were determined from carbon tracker (version CT2023; NOAA ESRL; http://carbontracker.noaa.gov; Peters et al., 2007). Clear-sky downwelling longwave radiances (W/[m^2 str cm^{-1}]) were then computed using the line-by-line radiative transfer model (LBLRTM; Clough & Iacono, 1995) at zenith angles of 0°, 20°, 40°, 60°, and 80° for the spectral range of the pyrgeometer (238–2,222 cm^{-1}). Computed radiances were fit to a quartic polynomial and integrated over the cosine of the zenith angle and over wavenumber giving the DLW radiative flux (W m^{-2}).

3.3. Downward Cloud Forcing

Computing cloud forcing requires the clear sky downwelling flux. Because radio soundings were infrequent, clear-sky downwelling fluxes were computed from the ERA5 reanalysis at hourly resolution from the 0.25-degree horizontal resolution output at the closest grid point (62.25°S, 59.0°W) to Escudero Station (62.2014°S, 58.9622°W). These are accumulated over the hour and reported in units of J m^{-2} at the end of the hour. After dividing each value by the number of seconds per hour, they therefore represent the average downwelling flux (W m^{-2}) over each hour. ERA5 clear sky fluxes interpolated to radio sounding times were found to agree well with clear sky downwelling fluxes computed using radio sounding profiles with a bias of −0.8 W m^{-2} and standard deviation of 4 W m^{-2}.

For calculating monthly average DLW and DSW forcings, measured fluxes were first averaged over each hour. The ERA5 hourly clear-sky fluxes were then subtracted from the averaged measured DLW and DSW fluxes yielding the DLW and DSW forcings. Months with measurements during fewer than 200 hr were excluded from the analysis; Figure S2 in Supporting Information S1 shows the number of hourly averaged measurements per month.

For categorizing the cloud type associated with DLW and DSW forcings using miniMPL measurements, first the DLW clear-sky fluxes from ERA5 were interpolated from the hourly time grid onto the time grid of the miniMPL

Table 1
Amount of Lidar Column Measurements Retained When Requiring That Each Column Measurement Type Match Column Measurement Types Within the Given Time Window

	30 min window		150 min window	
Classification	>50% match	>90% match	>50% match	>90% match
Clear Air	84%	53%	64%	26%
Liquid	98%	83%	95%	67%
Ice	88%	56%	68%	24%
Unknown Cloud	32%	3%	4%	0%
Obscured	86%	58%	72%	34%

measurements. Before interpolating, the ERA5 time grid was shifted back 30 min based on the assumption that the average over the hour would be most similar to the instantaneous values at the middle of the hour. The DLW forcing every 2 min was then computed as the measured DLW flux minus the interpolated clear-sky fluxes derived from ERA5.

The broadband DSW and DLW fluxes are hemispheric measurements, whereas the column categorization made by the lidar is range resolved but at a single latitude and longitude. It is therefore not necessarily a good approximation to assume that a single column measurement can be extrapolated to the whole hemisphere of the sky. To examine how heterogeneous the sky was in terms of cloudiness and cloud phase, we determined how representative a time window around each lidar column measurement was compared to the measurement itself based on the rationale that the variability in clouds passing over the instrument with time can be used as a proxy for spatial variability. Thus if liquid-containing clouds are observed for a consistent period of time, it is a fair estimate that such clouds cover a large portion of the sky. If conversely a single liquid column is observed surrounded in time by clear air, it seems likely that the sky cover was inhomogeneous.

To perform the analysis, we looked at a time window around each measurement and determined whether that measurement would be retained if a certain percentage (say 50%) of the data in the time window was required to have the same categorization. This was repeated for each column measurement to determine the percentage of data for which that percentage of the data in the time window was the same. The entire process was repeated using different percentage requirements and time windows. Selected results for 50% and 90% data consistency at 30 and 15 min are given in Table 1 (Figure S3 in Supporting Information S1 shows the results for time windows from 5 to 180 min in increments of 5 min and for consistency requirements of 1% to 100% with increments of 1%).

4. Cloud Characterization

4.1. Cloud Phase and Amount

Figure 2 shows the miniMPL measurements and derived cloud mask from 2022/12/28 to 2022/12/31 on KGI. Panel (c) shows the cloud mask profile with altitude. Thick low-level liquid (blue) and ice (red) clouds can be seen around 1 km during 12/29 and 12/30. This thick cloud attenuates the laser; the white region above the cloud indicates regions where there is insufficient signal for classification. The observable range is scene dependent; typically clouds limit characterization to the first few kilometers although the laser occasionally penetrates as high as 10 km. Cloud of unknown phase is indicated in gray (seen just before the start of 12/31 at about 3 km).

Based on the pixel-by-pixel cloud mask shown in panel (c), the cloud mask is derived for the atmospheric column as shown in panel (d). The column is classified as liquid-containing if there is liquid anywhere in the column. Thus, this can refer to multiple cloud layers with different phases, as seen during 12/29, where there is liquid at around 1 km (blue) and ice from 6 to 8 km (red) or to a single contiguous cloud containing both liquid and ice as seen on 12/31. The obscured classification ("Obsc.") refers to observations when the laser could not penetrate through the near-surface atmosphere likely due to a thick fog or precipitating cloud.

The column cloud mask during 2017–2023 is shown for each month as a function of year (symbols) and for the weighted mean of yearly results (colors) in Figure 3. There is a paucity of symbols during Austral winter, when the lidar was not operating most years.

Table 2 presents the frequencies of cloud mask categories annually and by season, excluding the "Obscured" and "Unknown Cloud" categories, as detailed in the Methods section." Skies are clear only 4% of the time overall with liquid observed in the atmospheric column most of the time. Liquid-containing clouds are prevalent all year. Clear skies and ice-only clouds occur slightly more (26%) in winter compared to other seasons (17%–22%).

Overall, the miniMPL identified clouds 96% of the time. In summer (DJF), clouds were observed 97% of the time. Compared to the raDAR/liDAR (DARDAR) MASK product for 2007–2010 (Listowski et al., 2019) for the pixel including Escudero Station, the total cloud amounts from the miniMPL were about 5% higher (DARDAR gives fractions of 85%–90% for DJF and MAM and 80%–85% for JJA and SON).

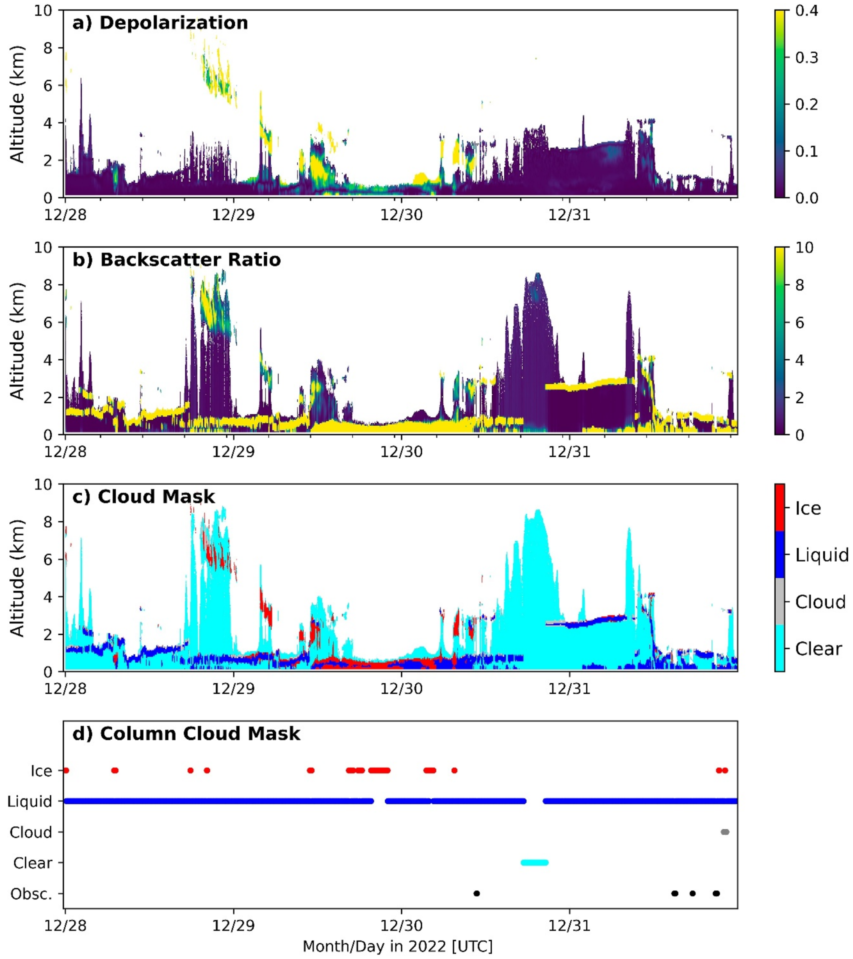

Figure 2. Mini micropulse lidar depolarization (a) and backscatter ratio (b) over King George Island from 2022/12/28 to 2022/12/31. Panel (c) gives the cloud mask determined from the depolarization and backscatter ratio where "Cloud" indicates clouds of indeterminate phase. For panel (d), the entire atmospheric column is categorized at each time step as described in the text. Time periods when the lidar laser is attenuated very close to the instrument are classified as obscured (Obsc.).

Our results are also considerably higher than the cloud occurrences observed during CAPRICORN (76%) in the region from 42 to 54°S (140 to 152°E; Mace & Protat, 2018). Similarly, for clouds with bases within the first 3 km (97% of miniMPL observations, as discussed below), our cloud occurrences are 45% higher than observations of low clouds made in the Southern Ocean at Macquarie Island (54.4°S, 158.9°E; Tansey et al., 2023) where low clouds were found to occur about 65% of the time on average (Note however that they refer to clouds with tops rather than bases within the first 3 km, so the frequencies are not perfectly comparable). At Macquarie Island, clouds were observed 10% less often in summer than winter; whereas at KGI, we observed slightly more clouds in summer (97% in summer compared to 95% in winter). These results are in line with expectations, given that KGI is farther south (62.2°S) and thus exposed to the circumpolar westerly winds from the South Pacific Ocean. Because of this, it is expected that these point observations are broadly representative across high-latitude areas over the Southern Ocean.

It is difficult to put error bounds on the miniMPL results or to determine how well we can extrapolate to the climatology more generally, given the small amount of data, particularly for winter. Symbols in Figure 3 give a sense of the year-to-year variability when observations were made. The standard deviation in the amount of clear sky observations over year varies from 0.9 to 4 (for months with multiple years represented), and the overall standard deviation is 2%. Additional measurements are needed to refine this result.

Journal of Geophysical Research: Atmospheres

10.1029/2024JD042787

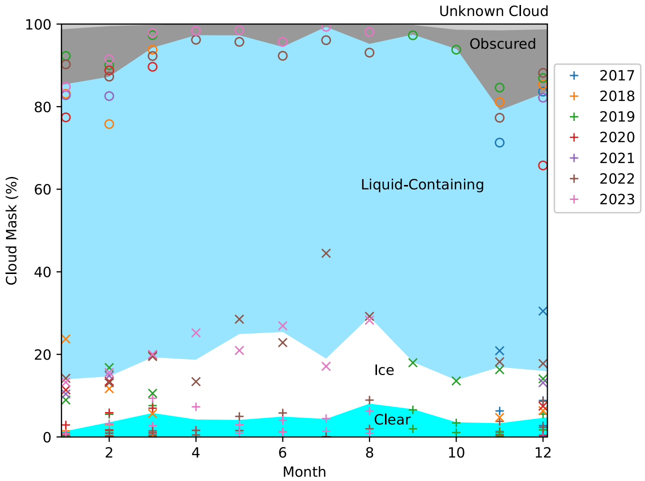

Figure 3. Clear-sky and phase classification for the atmospheric column above the mini micropulse lidar operating at Escudero Station from 2017 to 2023 for each month where the percentage of time is indicated by the vertical span. Averages for each year are represented by symbols: pluses indicate clear sky, crosses (x) indicate ice, and circles indicate liquid. The year is indicated by color, as shown in the legend. Obscured (dark gray) refers to time periods when the lidar could not penetrate far into the atmosphere. Unknown cloud (light gray) refers to times when the cloud phase could not be determined.

4.2. Lowest Cloud Base Height and Temperature

The LCBs observed by the miniMPL over Escudero were found to typically be very low, with 69% within the lowest 500 m of the atmosphere, 86% within the lowest 1 km, and 97% within the first 3 km. Figure 4 shows the distributions of the LCBs for liquid and ice. For liquid-containing clouds, nearly all LCBs were within 4 km (1.3% were above 4 km), whereas for ice-only clouds, 6.3% were above 4 km. It was possible to identify the lowest cloud bases (LCBs) for 90.3% of the cloudy-sky miniMPL results, when the lidar view was not obscured. This corresponds to worst case uncertainty ranges of 62%–72% for the lowest 500 m, 77%–87% for the lowest 1 km, and 87%–97% for the first 3 km.

The LCB height determines the LCB temperature. Figure 5 shows the temperature, taken from ERA5, at the LCB for each season and for liquid-containing and ice-only clouds. Most LCB temperatures fall within the range of 240–273 K, where both ice and supercooled liquid are possible. Some ice clouds were identified at temperatures above 273 K; these are either misidentified liquid clouds or indications that the temperature profile was incorrect. We assumed the latter was true for LCB temperatures up to 276 K, since cloud base temperatures are assumed to have an uncertainty of 3 K based on comparison of ERA5 to temperature profiles (We thus use an upper bin of 276 K for the highest bin edge for the ice-only cloud distribution). Almost no liquid-containing clouds are found at temperatures below about 240 K, as expected. Compared to liquid, there is a greater fraction of ice clouds at higher altitudes and lower temperatures.

5. Cloud Forcing

5.1. Monthly Mean Cloud Forcing

Figure 6 shows the monthly mean cloud forcing for DSW, DLW, and the total downwelling (DSW + DLW) for each year from 2017 to 2023 and for the mean over 2017–2023 (As described in the methods, cloud forcing is calculated from the difference between the measured downwelling radiation and the clear-sky radiation; these are given for reference in Figure S4 in Supporting Information S1). The seasonal cycle in DLW forcing is weak. Overall, clouds cause a cooling effect (negative forcing) during October–March, when sun angles are higher and shortwave cooling dominates and a warming during April–September, when longwave warming dominates.

5.2. Sensitivity of Cloud Forcing to Cloud Mask

Given accurate characterization of the atmosphere, cloud forcing is expected to be zero under clear skies. Here, however, DLW cloud forcing was determined from the broadband longwave radiation instrument, which has a hemispheric view of the atmosphere, whereas the cloud mask was determined from miniMPL measurements, which receives scattered light from a laser beam traversing a narrow column of the atmosphere. Thus, the two instruments view different regions of the atmosphere. Indeed, as shown in panel a of Figure 7, DLW cloud forcings can be significantly greater than zero when the miniMPL observes clear skies. Despite this limitation, large differences exist between the cloud forcing distributions for clear skies compared to time periods when the miniMPL observed liquid-containing or ice-only clouds (panels b and c), indicating the usefulness of comparing cloud forcings by cloud mask categories.

Table 2
Seasonal Occurrence of Cloud Mask Categories as Determined by the Micropulse Lidar Operating at Escudero Station From 2017 to 2023

	Occurrence (%)				
Cloud mask	Overall	Summer	Fall	Winter	Spring
Clear	4	3	5	6	4
Liquid-containing	80	83	79	75	83
Ice-only	16	14	17	20	13

Figure 7d shows the cloud forcing distribution for obscured cases and the small fraction of clouds for which phase could not be identified (indicated in the legend as unknown). The distribution of cloud forcing for obscured cases is dominated by high cloud forcing values, providing strong evidence

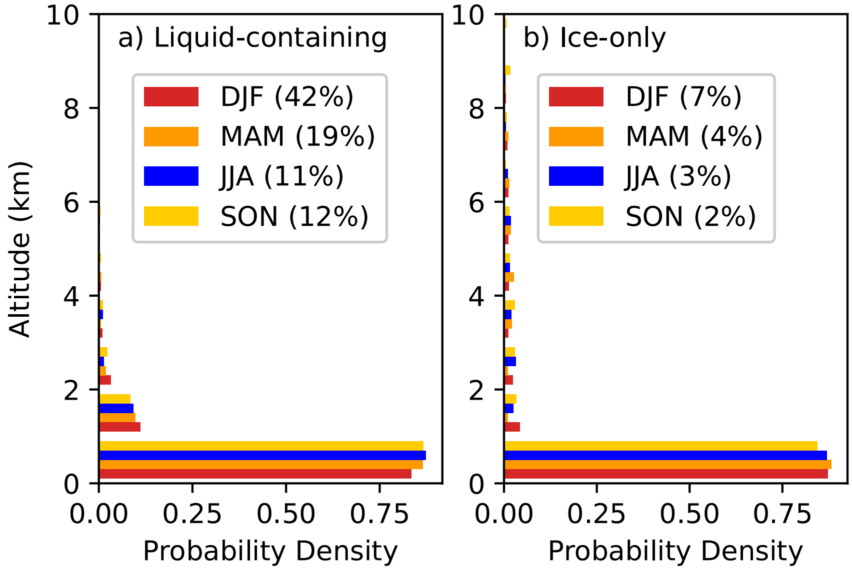

Figure 4. Lowest cloud base altitudes observed by the mini micropulse lidar by season (legend) over the years 2017–2023, for (a) liquid-containing clouds, and (b) ice-only clouds for each season as given in the legend. The legend also gives the percentages of the total amount of lowest clouds observed. Data are binned over 1 km with bin edges at integer numbers.

that most obscured cases occur when the sky is cloudy (i.e., precipitation is obscuring the laser rather than condensation). Thus, during time periods categorized as obscured, we assume clouds of unknown phase were present.

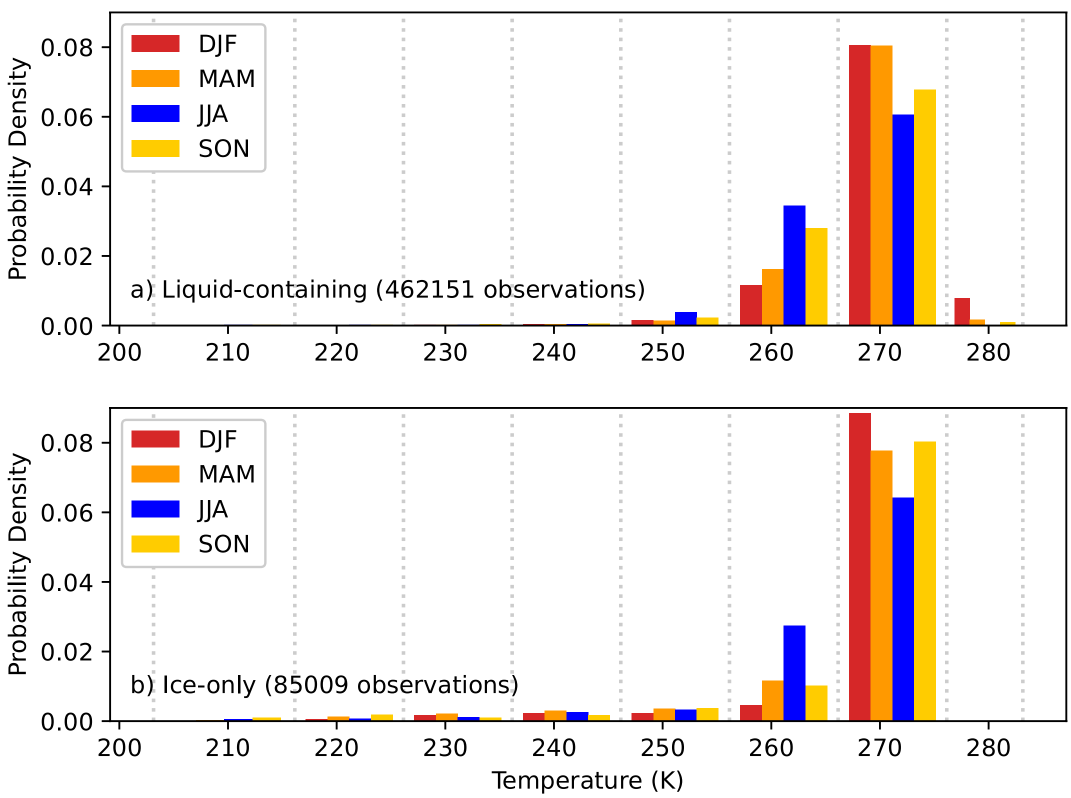

Figure 5. Temperature of the lowest cloud base determined from the mini micropulse lidar over the years 2017–2023, for each season, for (a) liquid-containing clouds, and (b) ice-only clouds. Bin edges are indicated with vertical dotted lines.

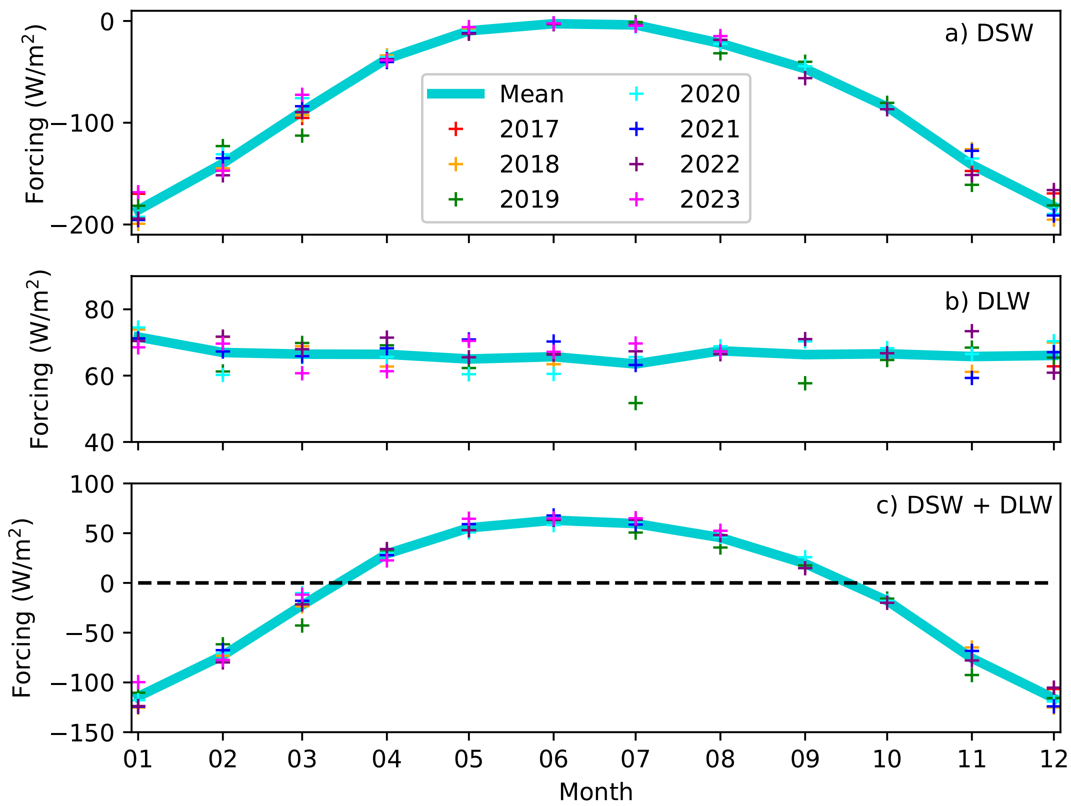

Figure 6. Monthly averages of (a) downwelling shortwave cloud forcing (DSW Forcing), (b) downward longwave cloud forcing (DLW), and (c) total downwelling cloud forcing measured at the surface at Escudero Station. Solid lines give weighted means of available data over 2017–2023. Symbols give monthly mean values for different years (see legend, which also corresponds to panel b).

Contrary to the expectation that ice clouds are generally optically thinner than liquid-containing clouds in the Antarctic (Lubin et al., 2015, 2020), which would lead to lower cloud forcing, the distributions of cloud forcing for liquid-containing and ice-only clouds are very similar. In fact, there is a greater proportion of low cloud-forcing values for liquid-containing clouds than for ice-only clouds with means of 67 and 75 W m^{-2}, respectively, and medians of 76 and 80 W m^{-2}. By comparison, Cox et al. (2014) found ice-only optical depth distributions in the Arctic to be shifted to higher values than liquid-only clouds but to lower values than mixed-phase clouds.

5.3. Sensitivity of Cloud Forcing to Cloud Phase and Temperature

To examine differences in the distributions for liquid-containing and ice-only clouds, Figure 8 shows the DLW cloud forcing distributions color-coded according to LCB temperature. Note that a significant number of clouds categorized as ice-only have temperatures between 273 and 276 K. As described in the methods, this difference is within the uncertainty of the ERA5 temperatures and thus we assumed these classifications were correct. A small fraction of the cloudy-sky observations (2,354, or 0.4%) was classified as ice-only despite LCB temperatures above 276 K. These were assumed to be liquid-containing and were included in panel a.

For clouds with base temperatures above 260 K, distributions are similar for liquid and ice, except that there is a greater proportion of low cloud-forcing values for liquid clouds with peaks at 85 W m^{-2} for both but a mean of 68 W m^{-2} for liquid and 79 W m^{-2} for ice. For clouds with base temperatures between 240 and 260 K, distributions are shifted toward lower values. This shift is greater for ice-only than for liquid-containing clouds: the peaks occur at about 45 W m^{-2} for ice compared to 65 W m^{-2} for liquid-containing clouds. For clouds with base temperatures below 240 K (for which liquid-containing clouds are negligible), the distribution is further shifted to lower values with a peak of 15 W m^{-2}.

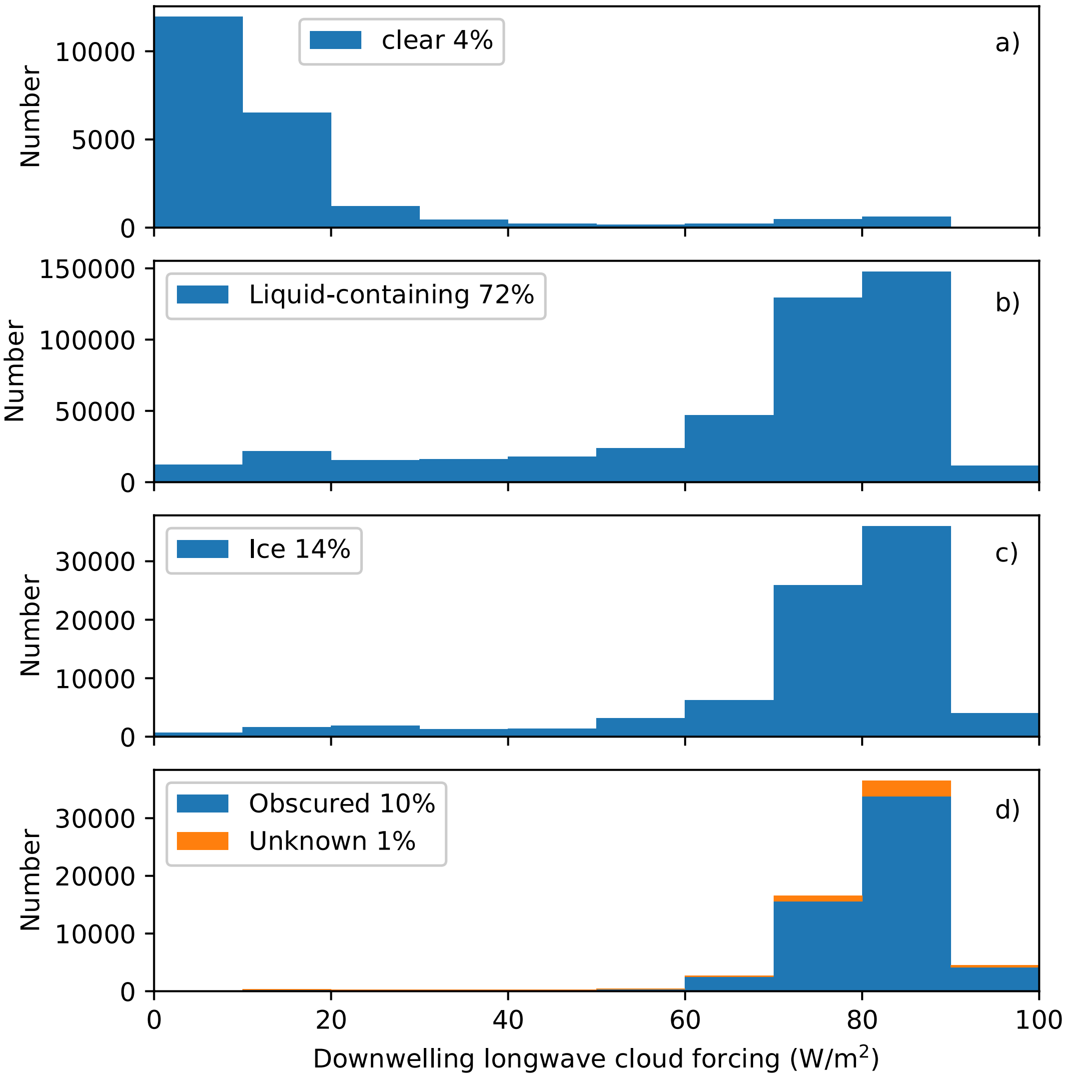

Figure 7. Downwelling longwave cloud forcing corresponding to mini micropulse lidar observations of (a) clear skies, (b) liquid-containing clouds, (c) ice-containing clouds, and (d) obscured cases and cases with clouds of uknown phase. Percentages of the total number of cases are given for each category in the leged.

Because cloud base temperatures are strongly correlated with base height with lower clouds typically warmer, distributions for cloud base heights follow a similar pattern, as shown in Figure S5 in Supporting Information S1.

Thus for the warmer (temperature $\geq$ 260 K), near-surface clouds (and clouds of unknown temperature), cloud forcings are high for both liquid-containing and ice-only clouds. It is possible that ice-only clouds with LCBs at pressures where ERA5 suggested temperatures were between 273 and 276 were misclassified and actually contain liquid. However, our conclusion still holds for ice-only columns with temperatures between 260 and 273 K. It is only for higher and colder clouds (temperature < 260 K) that ice-only clouds are found to have lower cloud forcing (by about 25 W m^{-2} for clouds between 240 and 260 K).

6. Cloud Forcing During Atmospheric Rivers

Because of extreme differences in daily insolation, which lead to differences in the relative amounts of shortwave and longwave radiation, it is useful to consider cloud forcing during strong ARs separately for summer and winter.

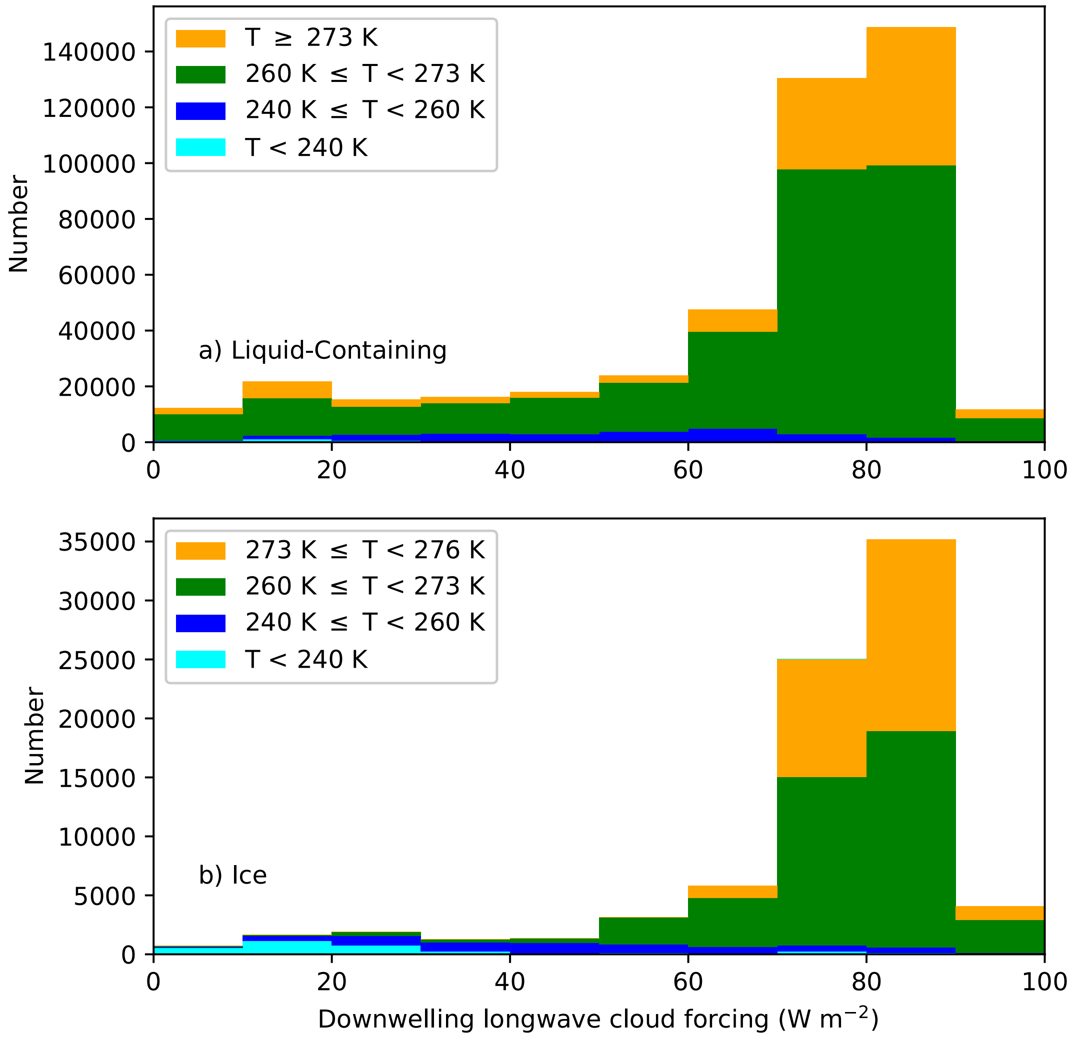

Figure 8. Downwelling longwave cloud forcing distributions over 2017–2023 at Escudero Station for (a) liquid-containing clouds and (b) ice-only clouds. Colors separate the distributions according to temperature at the cloud base (T) as indicated in the legend.

6.1. Summertime ARs

There were 11 strong ARs (AR1 or greater on the Polar AR Scale; see Zhang et al., 2024) identified at Escudero Station during summers (December–February) between 2017 and 2023. The mean cloud forcing during each AR is shown in Figure 9 as a function of surface temperature (green circles) together with daily mean cloud forcings for all summer measurements (blue circles). Mean values over all summertime ARs and over all daily means are given in the legend. Note that DSW values are all negative (panel a), indicating a SW cloud cooling effect, whereas DLW values are all positive (panel b), indicating a LW warming effect. Although these partially offset each other, the magnitude of the DSW flux is greater, such that the overall effect is a negative forcing, indicating cooling (panel c). During strong summertime ARs, cloud forcing was found to be weaker (closer to zero) than for summers overall by 16 W m^{-2} for DSW and 5 W m^{-2} for DLW. Because the DSW and DLW forcings have opposite signs, as discussed previously, this led to a total cloud forcing that was 10 W m^{-2} weaker during ARs. Given that ARs bring additional moisture, the opposite effect is expected. However, it is important to note that the result found here is speculative given the small number of strong ARs and the importance of solar zenith angle to the DSW effect, which translates to a sensitivity to the timing of ARs.

For the summer overall, no statistically significant correlation was found between surface temperature and cloud forcing (Surface temperatures were measured about a mile away from Escudero Station at Frei Station).

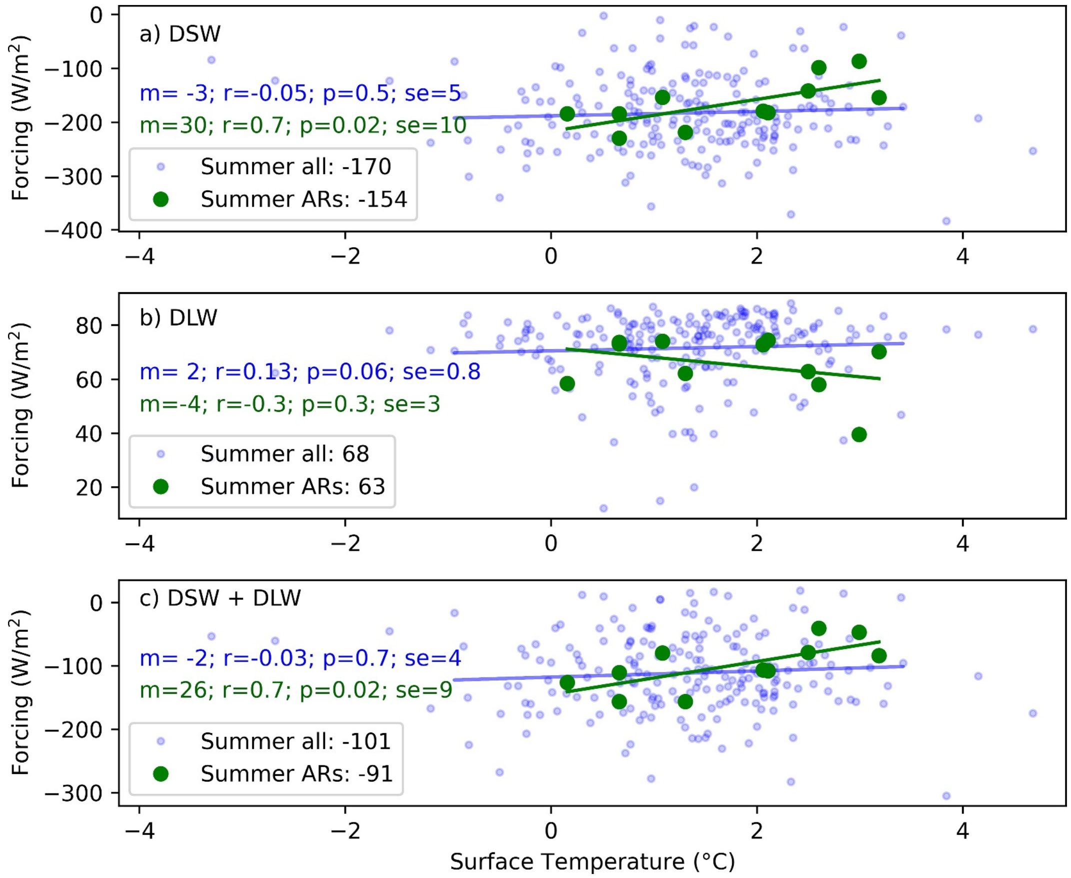

Figure 9. Scatter plot of daily mean surface temperature and cloud forcing measurements made at the surface at Frei and Escudero Stations (respectively) on King George Island during summers from 2017 to 2024 (blue points) together with mean values during strong summertime AR events (green circles). Panels show downward shortwave (DSW), downward longwave (DLW), and total (DSW + DLW) cloud forcing. Best fit lines are also shown and text gives the slope (m), Pearson's r, p-value (p), and standard error (se) for all summer (blue) and summertime ARs (green).

However, during summertime ARs, there is a statistically significant trend of higher surface temperatures with higher (i.e., weaker) DSW cloud forcing with an increase of 30 W m^{-2} in DSW cloud forcing for every one-degree temperature increase ($r^2 = 0.5$; $p = 0.02$; see Figure 9). Note that DSW is negative, meaning that less sunlight reaches the surface when clouds are present. Thus higher DSW values (which are closer to 0) imply weaker cloud forcing. It makes sense that weaker cloud forcing is found to correspond to higher surface temperatures during ARs because more sunlight is getting through the clouds. What is less clear is why a similar trend is not found for the summer as a whole. Because the DSW forcing is so strong in summer, the trend is nearly the same for the total downward cloud forcing (DLW + DSW). This indicates that summertime clouds mitigate the warming brought by ARs.

6.2. Wintertime ARs

There was one strong AR in the fall (May) and four in winter (June–August). Hereafter, we refer to these collectively as "wintertime ARs" for convenience.

In winter, cloud forcing was found to be stronger during ARs than for winter overall with DSW lower by 8 W m^{-2} and DLW forcing higher by 5 W m^{-2}. However, the small number of wintertime ARs suggests that additional measurements are needed to draw conclusions.

Identifying trends in cloud forcing with surface temperature during winter ARs is considerably more challenging compared to summer. There were only a small number of wintertime AR occurrences during the study period. In addition, in winter at the latitude of KGI, the DLW and DSW are of comparable magnitudes (e.g.,

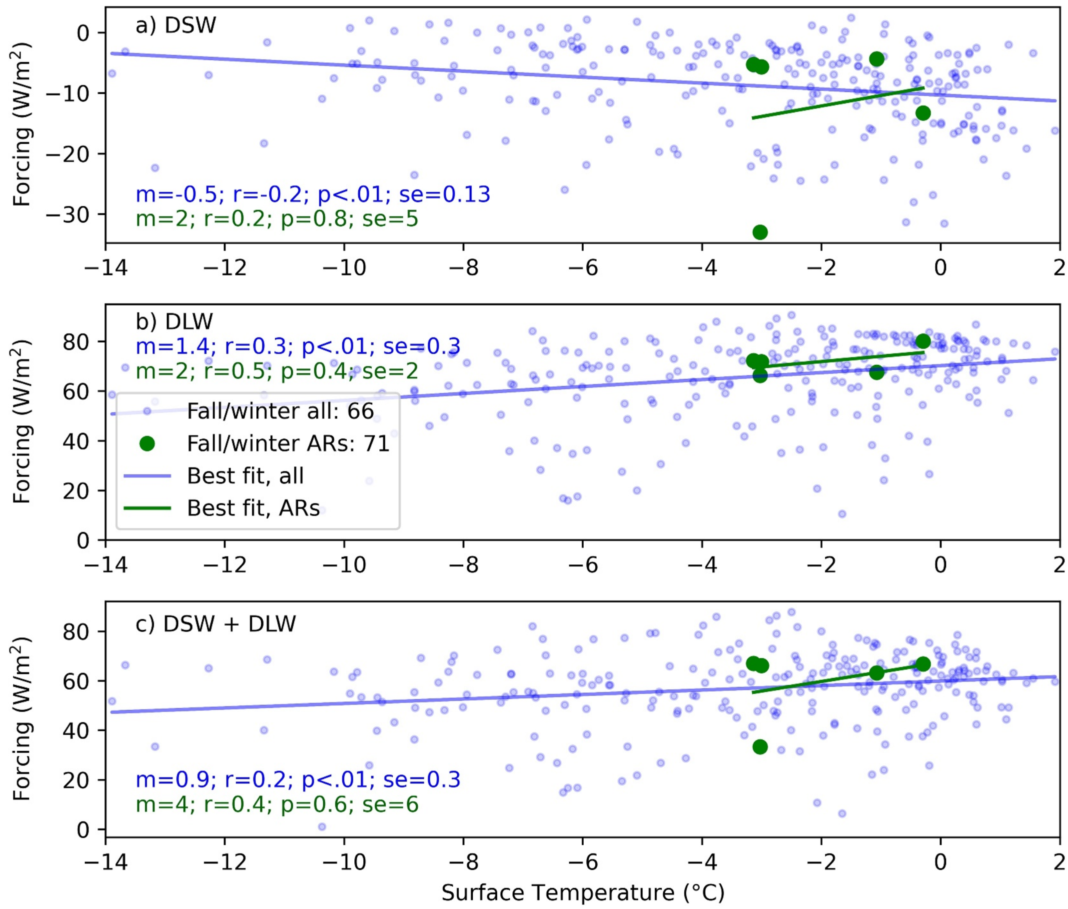

Figure 10. Scatter plot of daily mean surface temperature and cloud forcing measurements made at the surface at Frei and Escudero Stations (respectively) on King George Island during May–August from 2017 to 2024 (blue points) together with mean values during strong summertime AR events (green circles). Panels show downward shortwave (DSW), downward longwave (DLW), and total (DSW + DLW) cloud forcing. Best fit lines are also shown and text gives the slope (m), Pearson's r, p-value (p), and standard error (se) for all May–August (blue) and May–August ARs (green).

consider the y-axis on Figure 10, showing a range of 30 W m^{-2} for DSW and 100 W m^{-2} for DLW). Because they have opposite signs, the negative DSW cloud forcing and the positive DLW forcing cancel each other to a large degree, making trends with surface temperature weak. Given this, it is unsurprising that no statistically significant trends emerged between surface temperature and cloud forcing.

By contrast, for winter overall a statistically significant trend was found of increasing surface temperature with increasing DLW ($p < 0.01$; $m = 1$; Figure 10). Given the larger magnitude of the DLW compared to the DSW, a similar trend was found for DLW and total forcing. However, the r^2 value is only 0.04, indicating that the trend explains only a small fraction of the variability in the data. The small slope and low r^2 value make sense given the opposing DLW and DSW cloud forcing described above.

6.3. Implications

In summary, we find that summertime clouds mitigate the warming brought by ARs, whereas wintertime clouds enhance warming regardless of whether they are associated with an AR. The measurements made here are not sufficient to unambiguously determine the cause of these cloud forcing variations, which could be due to differences in cloud optical depth, temperature, or phase (liquid relative to ice).

Given the importance of ARs for extreme warming and melting events, this puts an important caveat on linkages between surface warming and cloud-induced increases in downward longwave radiation (e.g., Sato & Simmonds, 2021) particularly for the SO in summertime. KGI is farther north than the AP and therefore experiences higher sun angles. In addition, because the summertime SO is generally ice-free, reflected shortwave radiation is minimal. Taken together, this means that the DSW plays a much larger role in summer at KGI, causing summertime clouds to have a strong cooling effect during ARs. More work is needed to determine why a correlation is not found for summertime overall. In winter on KGI, the situation is more similar to that for the rest of Antarctica with clouds correlated with higher surface temperatures. However, this correlation explains less than 1% of the variation likely in part because solar radiation still plays a role albeit much smaller.

7. Conclusions

A suite of measurements made on King George Island in the Southern Ocean, just north of the Antarctic Peninsula, is used to characterize clouds over the annual cycle from 2017 to 2023. Based on micropulse lidar measurements, we find that clouds were present 96% of the time. These total cloud amounts are more than 5% higher than those given by the DARDAR mask product for 2007–2010 (Listowski et al., 2019) for the pixel including Escudero Station and for clouds below 3 km, about 45% higher than observations of low clouds made in the Southern Ocean at Macquarie Island (Tansey et al., 2023).

Low-level and supercooled liquid clouds are found to be common over King George Island. Most (86%) of the lowest cloud bases (LCBs) are within the first 1 km above the surface. Liquid-containing clouds are observed about 80% of the time, and temperatures at the LCBs are typically within the range where both liquid and ice are possible with cloud-base temperatures below 0°C for 82% of atmospheric columns classified as liquid-containing, indicating that most of the liquid cloud was supercooled. Low-level clouds for which the atmospheric column was classified as only containing ice are found to have a similar cloud forcing distribution as liquid-containing clouds, suggesting that ice-only clouds have similar optical thicknesses as liquid clouds, although optical depth measurements for ice and liquid clouds are needed to quantitatively determine if this is the case.

Monthly average downward cloud forcing is found to vary over the annual cycle from -116 W m^{-2} in December to 63 W m^{-2} in June and is found to be negative overall from October to March and positive overall from April to September. The cloud forcing distribution for low, warm ice clouds ($T > 260$ K) are found to be similar to that for liquid clouds, whereas ice clouds below 260 K are found to have lower cloud forcings. During the summer, surface temperatures are positively correlated with DSW cloud forcing during strong ARs explaining about 50% of the variance seen.

The surface-based lidar measurements made at King George Island are the only long-term lidar measurements that have been made near the northern edge of the Antarctic Peninsula over multiple seasons. These results therefore fill an important gap in our knowledge of clouds over the Southern Ocean. King George Island is in an important but understudied region. Its unique position, influenced by the circumpolar westerly winds, makes the measurements made there broadly representative of the larger ocean region. In addition, King George Island is in close proximity to the northern edge of the Antarctic sea ice zone where the sea ice expansion is influenced by the cloud-modulated downward longwave radiative flux (Cerovecki et al., 2022).

Overall, these results point to a need for additional measurements both in general and for targeted observations such as those needed for atmospheric rivers. More observations of the type presented would increase the statistical significance of some of the findings presented. Additionally, in situ measurements through clouds to better characterize cloud liquid, ice water content, and optical thickness would be helpful to understand how clouds and their interactions with radiation differ during atmospheric rivers and quantify biases in reanalysis data and model simulations, including future projections under climate change.

Data Availability Statement

Escudero cloud mask data derived from the micropulse lidar are available from Stillwell et al. (2025), Escudero radio sounding data from Rowe et al. (2025a), Escudero downward longwave radiative fluxes from Rowe et al. (2025b), and Escudero shortwave radiative fluxes from Rowe et al. (2025c). ERA5 reanalysis data are available from Copernicus Climate Change Service (2023). Software used for analysis and figure creation is available from Rowe (2025). Figures were created with matplotlib in Python.

Acknowledgments

We are grateful to the three anonymous reviewers of this manuscript for their helpful comments and suggestions, to the Instituto Antártico Chileno (INACH) for supporting research at the Chilean Antarctic Station, Escudero, and to the many students and others who helped collect data and maintain the platform at Escudero Station, including N. Dettling, J. Jorquera, F. Cabello, J. Carrera, and B. Valdevenito. We thank J. Carrasco for helping obtain Chilean Meteorological data. CO_2 concentrations used in the creation of atmospheric profiles were from CarbonTracker (version CT2023, NOAA ESRL; http://carbontracker.noaa.gov; Peters et al., 2007). We are grateful to Peter Kuma for sharing the mpl2nc codebase used to convert micropulse lidar output files to netcdf files. Material derived from analysis of the micropulse lidar data is based upon work supported by the NSF National Center for Atmospheric Research, which is a major facility sponsored by the National Science Foundation under Cooperative Agreement No. 1852977. This work was funded by National Science Foundation Grants 2127632, 2205398, and 2229392 and by Fondecyt 1161460. R.R. Cordero acknowledges USACH-DICYT 092431CC_Ayudante and Fondecyt 1231904. I. Gorodetskaya acknowledges support from Portuguese FCT for strategic funding to CIIMAR (UIDB/04423/2020, UIDP/04423/2020), CEEC IND IMPACT (2021.03140.CEECIND/CP1659/CT0005), and Portuguese Polar Program.

References

Bodas-Salcedo, A., Williams, K. D., Field, P. R., & Lock, A. P. (2012). The surface downwelling solar radiation surplus over the Southern Ocean in the Met Office model: The role of midlatitude cyclone clouds. *Journal of Climate*, *25*(21), 7467–7486.

Bodas-Salcedo, A., Williams, K. D., Ringer, M. A., Beau, I., Cole, J. N., Dufresne, J. S., et al. (2014). Origins of the solar radiation biases over the Southern Ocean in CFMIP2 models. *Journal of Climate*, *27*(1), 41–56.

Bozkurt, D., Rondanelli, R., Marín, J. C., & Garreaud, R. (2018). Foehn event triggered by an atmospheric river underlies record-setting temperature along continental Antarctica. *Journal of Geophysical Research: Atmospheres*, *123*, 3871–3892. https://doi.org/10.1002/2017JD027796

Bromwich, D. H., Werner, K., Casati, B., Powers, J. G., Gorodetskaya, I. V., Massonnet, F., et al. (2020). The year of polar prediction in the Southern hemisphere (YOPP-SH). *Bulletin of the American Meteorological Society*, *101*(10), E1653–E1676.

Campbell, J. R., Hlavka, D. L., Welton, E. J., Flynn, C. J., Turner, D. D., Spinhirne, J. D., et al. (2002). Full-time, eye-safe cloud and aerosol lidar observation at atmospheric radiation measurement program sites: Instruments and data processing. *Journal of Atmospheric and Oceanic Technology*, *19*(4), 431–442. https://doi.org/10.1175/1520-0426(2002)019<0431:FTESCA>2.0.CO;2

Cerovecki, I., Sun, R., Bromwich, D. H., Zou, X., Mazloff, M. R., & Wang, S.-H. (2022). Impact of downward longwave radiative deficits on Antarctic sea-ice extent predictability during the sea ice growth period. *Environmental Research Letters*, *17*, 084008. https://doi.org/10.1088/1748-9326/ac7d66

Clough, S. A., & Iacono, M. J. (1995). Line-by-line calculations of atmospheric fluxes and cooling rates. 2: Application to carbon dioxide, ozone, methane, nitrous oxide and the halocarbons. *Journal of Geophysical Research*, *100*, 16519–16535.

Copernicus Climate Change Service, Climate Data Store. (2023). ERA5 hourly data on pressure levels from 1940 to present. *Copernicus Climate Change Service (C3S) Climate Data Store (CDS)*. https://doi.org/10.24381/cds.bd0915c6

Cox, C. J., Turner, D. D., Rowe, P. M., Shupe, M. D., & Walden, V. P. (2014). Cloud microphysical properties retrieved from downwelling infrared radiance measurements made at Eureka, Nunavut, Canada (2006–09). *Journal of Applied Meteorology and Climatology*, *53*(3), 772–791.

Fernald, F. G., Herman, B. M., & Reagan, J. A. (1972). Determination of aerosol height distributions by lidar. *Journal of Applied Meteorology and Climatology*, *11*, 482–489. https://doi.org/10.1175/1520-0450(1972)011<0482:DOAHDB>2.0.CO;2

Fiddes, S. L., Protat, A., Mallet, M. D., Alexander, S. P., & Woodhouse, M. T. (2022). Southern Ocean cloud and shortwave radiation biases in a nudged climate model simulation: Does the model ever get it right? *Atmospheric Chemistry and Physics*, *22*(22), 14603–14630.

Flynn, C. J., Mendoza, A., Zheng, Y., & Mathur, S. (2007). Novel polarization-sensitive micropulse lidar measurement technique. *Optics Express*, *15*(6), 2785–2790. https://doi.org/10.1364/oe.15.002785

Gilbert, E., Orr, A., King, J. C., Renfrew, I. A., Lachlan-Cope, T., Field, P. F., & Boutle, I. A. (2020). Summertime cloud phase strongly influences surface melting on the Larsen C ice shelf, Antarctica. *Quarterly Journal of the Royal Meteorological Society*, *146*(729), 1575–1589.

Gorodetskaya, I. V., Durán-Alarcón, C., González-Herrero, S., Clem, K. R., Zou, X., Rowe, P., et al. (2023). Record-high Antarctic Peninsula temperatures and surface melt in February 2022: A compound event with an intense atmospheric river. *npj Climate and Atmospheric Science*, *6*, 202. https://doi.org/10.1038/s41612-023-00529-6

Grosvenor, D. P., Choularton, T. W., Lachlan-Cope, T., Gallagher, M. W., Crosier, J., Bower, K. N., et al. (2012). In-situ aircraft observations of ice concentrations within clouds over the Antarctic Peninsula and Larsen Ice Shelf. *Atmospheric Chemistry and Physics*, *12*(23), 11275–11294.

Haynes, J. M., Jakob, C., Rossow, W. B., Tselioudis, G., & Brown, J. (2011). Major characteristics of Southern Ocean cloud regimes and their effects on the energy budget. *Journal of Climate*, *24*(19), 5061–5080.

Hersbach, H., Bell, B., Berrisford, P., Biavati, G., Horányi, A., Muñoz Sabater, J., et al. (2023). ERA5 hourly data on pressure levels from 1940 to present. *Copernicus Climate Change Service (C3S) Climate Data Store (CDS)*. https://doi.org/10.24381/cds.bd0915c6

Hersbach, H., Bell, B., Berrisford, P., Hirahara, S., Horanyi, A., Muñoz-Sabater, J., et al. (2020). The ERA5 global reanalysis. *Quarterly Journal of the Royal Meteorological Society*, *146*(730), 1999–2049. https://doi.org/10.1002/qj.3803

Howat, I. M., Porter, C., Smith, B. E., Noh, M. J., & Morin, P. (2019). The reference elevation model of Antarctica. *The Cryosphere*, *13*(2), 665–674. https://doi.org/10.5194/tc-13-665-2019

Hu, Y., Rodier, S., Xu, K. M., Sun, W., Huang, J., Lin, B., et al. (2010). Occurrence, liquid water content, and fraction of supercooled water clouds from combined CALIOP/IIR/MODIS measurements. *Journal of Geophysical Research*, *115*(19), 937. https://doi.org/10.1029/2009JD012384

Huang, Y., Siems, S. T., Manton, M. J., Protat, A., & Delanoë, J. (2012). A study on the low-altitude clouds over the Southern Ocean using the DARDAR-MASK. *Journal of Geophysical Research*, *117*(17), D18204. https://doi.org/10.1029/2012JD017800

Hyder, P., Edwards, J. M., Allan, R. P., Hewitt, H. T., Bracegirdle, T. J., Gregory, J. M., et al. (2018). Critical Southern Ocean climate model biases traced to atmospheric model cloud errors. *Nature Communications*, *9*(1), 3625. https://doi.org/10.1038/s41467-018-05634-2

Klett, J. D. (1981). Stable analytical inversion solution for processing lidar returns. *Applied Optics*, *20*(2), 211–220.

Listowski, C., Delanoë, J., Kirchgaessner, A., Lachlan-Cope, T., & King, J. (2019). Antarctic clouds, supercooled liquid water and mixed phase, investigated with DARDAR: Geographical and seasonal variations. *Atmospheric Chemistry and Physics*, *19*(10), 6771–6808.

Lubin, D., Kahn, B. H., Lazzara, M. A., Rowe, P., & Walden, V. P. (2015). Variability in AIRS-retrieved cloud amount and thermodynamic phase over west versus east Antarctica influenced by the SAM. *Geophysical Research Letters*, *42*(4), 1259–1267. https://doi.org/10.1002/2014GL062285

Lubin, D., Zhang, D., Silber, I., Scott, R. C., Kalogeras, P., Battaglia, A., et al. (2020). AWARE in west Antarctica. *Bulletin of the American Meteorological Society*, *101*(10), 892–898.

Mace, G., & Protat, A. (2018). Clouds over the Southern Ocean as observed from the R/V investigator during CAPRICORN. Part I: Cloud occurrence and phase partitioning. *Journal of Applied Meteorology and Climatology*, *57*(8), 1783–1803. https://doi.org/10.1175/jamc-d-17-0194.1

McFarquhar, G. M., Bretherton, C. S., Marchand, R., Protat, A., DeMott, P. J., Alexander, S. P., et al. (2021). Observations of clouds, aerosols, precipitation, and surface radiation over the Southern Ocean: An overview of CAPRICORN, MARCUS, MICRE, and SOCRATES. *Bulletin of the American Meteorological Society*, *102*(4), E894–E928. https://doi.org/10.1175/BAMS-D-20-0132

NASA Micro-Pulse Lidar Network. (2023). Micropulse lidar data for Escudero station [Dataset]. Retrieved from https://mplnet.gsfc.nasa.gov/

O'Shea, S. J., Choularton, T. W., Flynn, M., Bower, K. N., Gallagher, M., Crosier, J., et al. (2017). In situ measurements of cloud microphysics and aerosol over coastal Antarctica during the MAC campaign. *Atmospheric Chemistry and Physics*, *17*(21), 13049–13070.

Peters, W., Jacobson, A. R., Sweeney, C., Andrews, A. E., Conway, T. J., Masarie, K., et al. (2007). An atmospheric perspective on North American carbon dioxide exchange: CarbonTracker. *Proceedings of the National Academy of Sciences*, *104*(48), 18925–18930.

Rowe, P. (2025). prowe12/antarctic-peninsula: Comparison of atmospheric observations over escudero to models: April 1, 2025 release (version 1.0.1) [Software]. *Zenodo*. https://doi.org/10.5281/zenodo.15117762

Rowe, P., Cordero, R., Zou, X., & Gorodetskaya, I. (2025a). Radiosonde measurements (King George Island), 2017 - 2023 [Dataset]. *AMRDC Data Repository*. https://doi.org/10.48567/jqv8-r657

Rowe, P., Cordero, R., Zou, X., & Gorodetskaya, I. (2025b). Longwave downward radiative flux (King George Island), 2017 - 2023 [Dataset]. *AMRDC Data Repository*. https://doi.org/10.48567/hnhz-f486

Rowe, P., Cordero, R., Zou, X., & Gorodetskaya, I. (2025c). Shortwave downward radiative flux (King George Island), 2017 - 2023 [Dataset]. https://doi.org/10.48567/peeg-7j35

Rowe, P. M., Miloshevich, L. M., Turner, D. D., & Walden, V. P. (2008). Dry bias in Vaisala RS90 radiosonde humidity profiles over Antarctica. *Journal of Atmospheric and Oceanic Technology*, *25*(9), 1529–1541.

Sato, K., & Simmonds, I. (2021). Antarctic skin temperature warming related to enhanced downward longwave radiation associated with increased atmospheric advection of moisture and temperature. *Environmental Research Letters*, *16*(6), 064059.

Stillwell, R., Rowe, P., Cordero, R., Zou, X., & Gorodetskaya, I. (2025). Cloud mask data (King George Island), 2017 - 2023 [Dataset]. *AMRDC Data Repository*. https://doi.org/10.48567/1wd1-ea27

Stillwell, R. A., Neely III, R. R., Thayer, J. P., Shupe, M. D., & Turner, D. D. (2018). Improved cloud-phase determination of low-level liquid and mixed-phase clouds by enhanced polarimetric lidar. *Atmospheric Measurement Techniques*, *11*, 835–859. https://doi.org/10.5194/amt-11-835-2018

Tansey, E., Marchand, R., Alexander, S. P., Klekociuk, A. R., & Protat, A. (2023). Southern Ocean low cloud and precipitation phase observed during the Macquarie Island Cloud and Radiation Experiment (MICRE). *Journal of Geophysical Research*, *128*, e2023JD039205. https://doi.org/10.1029/2023JD039205

Trenberth, K. E., Fasullo, J. T., O'Dell, C., & Wong, T. (2010). Relationships between tropical sea surface temperature and top-of-atmosphere radiation. *Geophysical Research Letters*, *37*(3), L03702. https://doi.org/10.1029/2009GL042314

Wille, J. D., Alexander, S. P., Amory, C., Baiman, R., Barthélemy, L., Bergstrom, D. M., et al. (2024). The extraordinary March 2022 East Antarctica “heat” wave. Part I: Observations and meteorological drivers. *Journal of Climate*, *37*(3), 757–778.

Wille, J. D., Favier, V., Dufour, A., Gorodetskaya, I. V., Turner, J., Agosta, C., & Codron, F. (2019). West Antarctic surface melt triggered by atmospheric rivers. *Nature Geoscience*, *12*(11), 911–916.

Zhang, Z., Ralph, F. M., Zou, X., Kawzenuk, B., Zheng, M., Gorodetskaya, I. V., et al. (2024). Extending the CW3E atmospheric river scale to the polar regions. *EGUsphere*, *2024*, 1–36. https://doi.org/10.5194/tc-18-5239-2024

Zou, X., Rowe, P. M., Gorodetskaya, I., Bromwich, D. H., Lazzara, M. A., Cordero, R. R., et al. (2023). Strong warming over the Antarctic Peninsula during combined atmospheric river and Foehn events: Contribution of shortwave radiation and turbulence. *Journal of Geophysical Research: Atmospheres*, *128*(16), e2022JD038138. https://doi.org/10.1029/2022JD038138